Application of tissue-scale tension to avian epithelia *in vivo* to study multiscale mechanical properties and inter-germ layer coupling

Panagiotis Oikonomou*, Lisa Calvary*, Helena C. Cirne, Andreas E. Welch, John F. Durel, Olivia Powell, Nandan L. Nerurkar#

Department of Biomedical Engineering, Columbia University, New York NY 10027

#Correspondence to: **nln2113@columbia.edu**

351 Engineering Terrace, 1210 Amsterdam Avenue, New York, New York 10027

Graphical Abstract

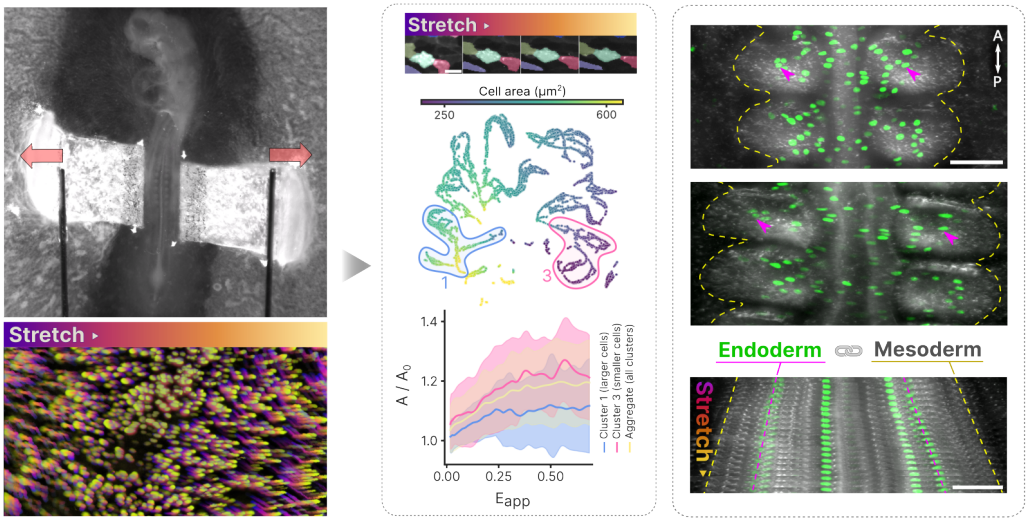

Summary Statement A simple approach is devised for quantitatively applying tension to epithelia *in vivo*, and used to study the mechanics of embryonic epithelia in the chick embryo.

ABSTRACT

As cross-disciplinary approaches drawing from physics and mechanics have increasingly influenced our understanding of morphogenesis, the tools available to measure and perturb physical aspects of embryonic development have expanded as well. However, it remains a challenge to measure mechanical properties and apply exogenous tissue-scale forces *in vivo*, particularly for epithelia. Exploiting the size and accessibility of the developing chick embryo, here we describe a simple technique to quantitatively apply exogenous forces on the order of ∼1-100 μN to the endodermal epithelium. To demonstrate the utility of this approach, we performed a series of proof-of-concept experiments that reveal fundamental and unexpected mechanical behaviors in the early chick embryo, including mechanotype heterogeneity among cells of the midgut endoderm, complex non-cell autonomous effects of actin disruption, and a high degree of mechanical coupling between the endoderm and adjacent paraxial mesoderm. To illustrate the broader utility of this method, we determined that forces on the order of ~ 10 μN are sufficient to unzip the neural tube during primary neurulation. Together, these findings provide basic insights into the mechanics of embryonic epithelia *in vivo* in the early avian embryo, and provide a useful tool for future investigations of how morphogenesis is influenced by mechanical factors.

KEYWORDS: epithelial mechanics, chick, endoderm, neurulation, cell morphometry

INTRODUCTION

Development requires coordination of cell fate specification with growth and mechanical forces that deform embryonic tissues into precise shapes and sizes. Accordingly, a mechanically motivated framework for studying development has provided increasingly cross-disciplinary insights, particularly over the past two decades. This physically-motivated view of development has revealed that mechanisms of morphogenesis can be understood using purely mechanical descriptions, providing insights even in the absence of implicating genes or signaling pathways per se (Mongera et al., 2018; Saadaoui et al., 2020; Savin et al., 2011; Serra et al., 2023; Shyer et al., 2013; Tallinen et al., 2014). At the same time, physical forces and mechanical properties have begun to be recognized as guiding cell behaviors and gene expression as well, revealing mechanics as an important upstream regulator of cell behaviors during development (Barriga et al., 2018; Farge, 2003). Therefore, mechanics has increasingly become woven into our understanding of morphogenesis both as an effector and modifier of developmental programs (Collinet & Lecuit, 2021). This has led to development of a range of tools for measuring forces and mechanical properties of embryonic tissue *in vivo* (Campàs et al., 2014; Chan et al., 2023; Dzementsei et al., 2022; Gómez-González et al., 2020; Mongera et al., 2018; Regev et al., 2022) as well as in explanted tissue (Barriga et al., 2018; Savin et al., 2011; Shyer et al., 2013; Zamir et al., 2003), (Shook et al., 2018), (Zhou et al., 2009). However, these efforts have primarily advanced the ability to study properties mesenchymal tissues, and it remains a challenge to apply exogenous tension to epithelia *in vivo*. In particular, approaches for applying and simultaneously measuring tissue-scale tension in embryonic epithelia are limited (Doubrovinski et al., 2017). As a result, mechanical behaviors of embryonic epithelia remain under-explored, particularly among amniotes.

Here, we describe a simple method to apply exogenous, uniaxial stretch to epithelia in the chick embryo *in vivo*. Focusing primarily on the presumptive midgut endoderm, we conducted a series of experiments investigating mechanical heterogeneity at both tissue and cell length-scales, and quantifying mechanical coupling between endoderm and mesoderm. Finally, to extend this beyond endoderm to other contexts, we applied tension to the ectoderm, quantifying the tensile forces necessary to unzip the forming neural tube. This approach has the potential to advance the measurement of physical properties of tissues *in vivo*, as well as the investigation of mechanical influences on morphogenesis.

RESULTS

In vivo application and measurement of tension to intact epithelia in the chick embryo

In order to study mechanical properties of the avian endoderm, we devised a simple approach for applying tension directly onto the flat endodermal epithelium of the presumptive midgut of chick embryos. We designed a simple apparatus that sits on a microscope stage, and consists of a linear actuator driving bidirectional displacement of a pair of fine tungsten cantilevers to apply tensile forces to the embryo (Fig. 1A). Optically monitoring bending of the cantilevers can be used to calculate the associated force, which varies linearly with deflection of the cantilever tip (Fig. S1A). Cantilevers of 0.13 mm diameter and 40 mm length were used to perform force measurements in the range of 1-1,000 μN. To transmit displacement of the paired tungsten rods to stretching of the endoderm, we used an approach motivated by EC culture (Chapman et al., 2001), placing small L-shaped pieces of filter paper along the lateral edges of the presumptive midgut region of the embryo at Hamburger Hamilton (HH) stage 13, such that they contacted only the hypoblast and the lateral margin of gut-forming endoderm (Fig. 1B-D). Just as filter paper binds tightly to the vitelline membrane during EC culture, the filter paper squares adhered tightly to the ventral epithelium, such that when stretch was applied via lateral displacement of the paired tungsten rods, large 2-D tissue deformations could be directly observed when combined with endoderm-specific electroporation of plasmid DNA encoding a fluorescent reporter to visualize cell nuclei (Nerurkar et al., 2019) (Fig. 1E). Quantification of 2-D Lagrangian strains revealed a largely homogeneous strain field under applied stretch, with antero-posterior shortening (negative strains) accompanying large extensional (positive) strains along the medio-lateral axis (Fig. 1F, G). The endoderm was highly extensible, accommodating 50-70% stretch before showing macroscopic signs of rupture. Medio-lateral strains were similar between the medial gut-forming endoderm and lateral hypoblast regions, suggesting similar mechanical properties across these regions (Fig. S1B). Alignment of the directions of maximum and minimum principal strains with the medio-lateral and antero-posterior axes of the embryo, respectively, indicate that a simple biaxial deformation was achieved throughout the endoderm, with little to no shear (Fig. 1G).

Identification of single-cell mechanotypes through application of exogenous stretch

The ability to apply exogenous stretch to the endoderm *in vivo* provides access to a range of questions regarding the mechanical behaviors of embryonic epithelia, and the gut-forming endoderm in particular. Moving from the tissue-scale effects of stretch to the cellular

scale, we asked how applied macroscopic stretch is translated locally to cell deformations, relying on endoderm-specific electroporation of pCAG-EGFP-CAAX to visualize cell boundaries during application of exogenous stretch (Fig. 2A, Supplemental Movie S1). Automated cell segmentation (Stringer et al., 2020) and tracking (Ulicna et al., 2021) was used to quantify the evolution of single-cell morphometrics for hundreds of epithelial cells per embryo as stretch is progressively increased on the endoderm (Fig. 2B), enabling quantification of several features such as cell area, aspect ratio, orientation, strain, and position. To handle the large amount of data generated (20 features for each of approximately 20,000 cells across samples and movie frames), we employed UMAP (Uniform Manifold Approximation and Projection) to create a low-dimensional representation of the high-dimensional cell morphology measurements (See Methods) (Shannon et al., 2023). Cells were broadly distributed in the UMAP space, reflecting potential heterogeneity in the mechanical and morphological characteristics of endoderm cells. Cells from each of six embryos were well distributed in UMAP space, indicating that heterogeneity is not likely explained by embryo-to-embryo variability or batch effects (Fig. S2A). This led us to hypothesize that distinct "mechanotypes" exist in the dataset, i.e. populations of cells with distinct mechanical behaviors in response to external strain. To isolate potential mechanotypes, we performed unsupervised clustering of the cells by their similarity in features (accounting for morphometry, strain, etc.) using HDBSCAN (Fig. 2C), and confirmed that these clusters largely include entire cell trajectories, allowing us to

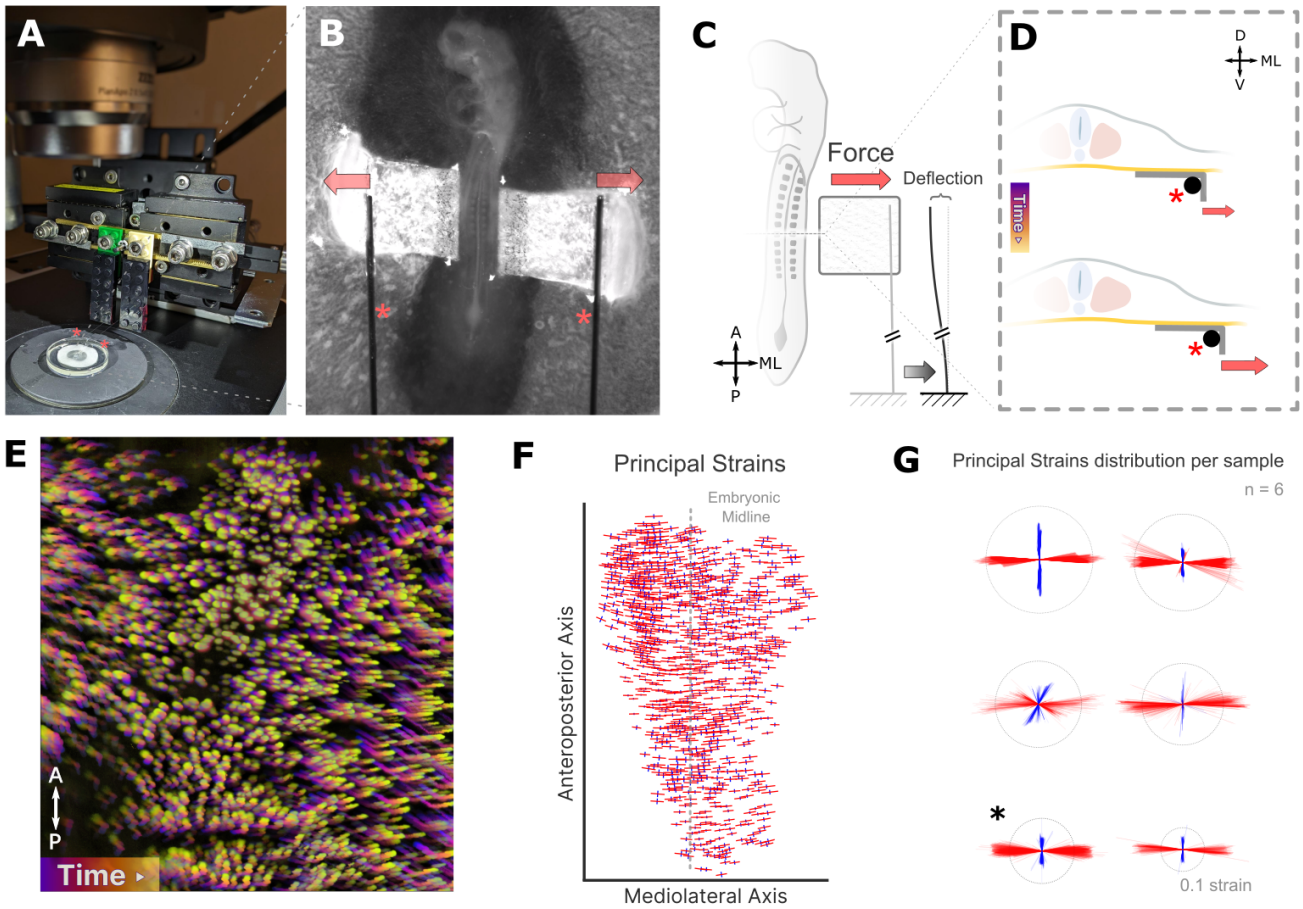

Figure 1. Schematic overview of apparatus and sample. (**A**) Stretching apparatus sitting atop the microscope stage, red asterisks denote the tungsten cantilevers. (**B**) Magnified view cantilevers bilaterally engaging "L-shaped" filter papers adherent to the endoderm. (**C**) Schematic representation of simultaneous stretching and force measurement via measurement of cantilever deflection. (**D**) Schematic transverse representation of the "L-shaped" filter paper attachment to endoderm and engaging the cantilever, which is displaced laterally to stretch the endoderm. (**E**) Color-coded time projection of applied deformation in endoderm following electroporation with pCAG-H2B-GFP to visualize endoderm cell nuclei. (**F**) Principal Lagrangian strains quantified for a representative embryo from tissue displacements under exogenously applied medio-lateral stretch; length and orientation of red/blue lines indicates the magnitude and orientation maximum/minimum principal strains, respectively. (**G**) Superposition of maximum (red) and minimum (blue) principal strains throughout the endoderm for 6 embryos; dashed circle indicates a strain magnitude of 0.1; *indicates representative embryo from (F).

study the evolution of features within a cluster as a function of applied strain (Fig. S2B). Plotting each feature on UMAP space (Fig. S2C), we observed that the dominant structure in the UMAP follows an axis of increasing cell areas (Fig. 2D, Fig. S3A), with a secondary axis of separation according to applied strain and associated changes in cell area (Fig. S2C). For each cell cluster, stretching increased both area and aspect ratio, and led to reorientation of cells toward the direction of applied tissue stretch (Fig. S3C). However, while aspect ratio increased linearly with applied stretch, area changes were nonlinear, plateauing after an initial dilatation (Fig. 2E ; Fig. S3C). Interestingly, we found that larger cells attenuate their area expansion at lower applied strains than smaller cells (Fig. 2E, Fig. S3B,C).

Endoderm-specific disruption of F-actin non cell-autonomously reduces tissue stiffness and cell area changes under tension

With the ability to apply tension to epithelia *in vivo*, one can test the contribution of specific subcellular components through targeted disruption of their normal function. As an example, we disrupted F-actin in a subpopulation of endoderm to examine how cell and tissue mechanics were altered. This was accomplished by electroporation to misexpress DeAct-SpvB (DeAct), a GFP-fused ADP-ribosyltransferase that induces actin depolymerization by disrupting the ability of G-actin monomers to polymerize (Harterink et al., 2017). To examine non cell-autonomous effects, a second electroporation was carried out to visualize neighboring cells by misexpression of a membrane localized RFP (myr-

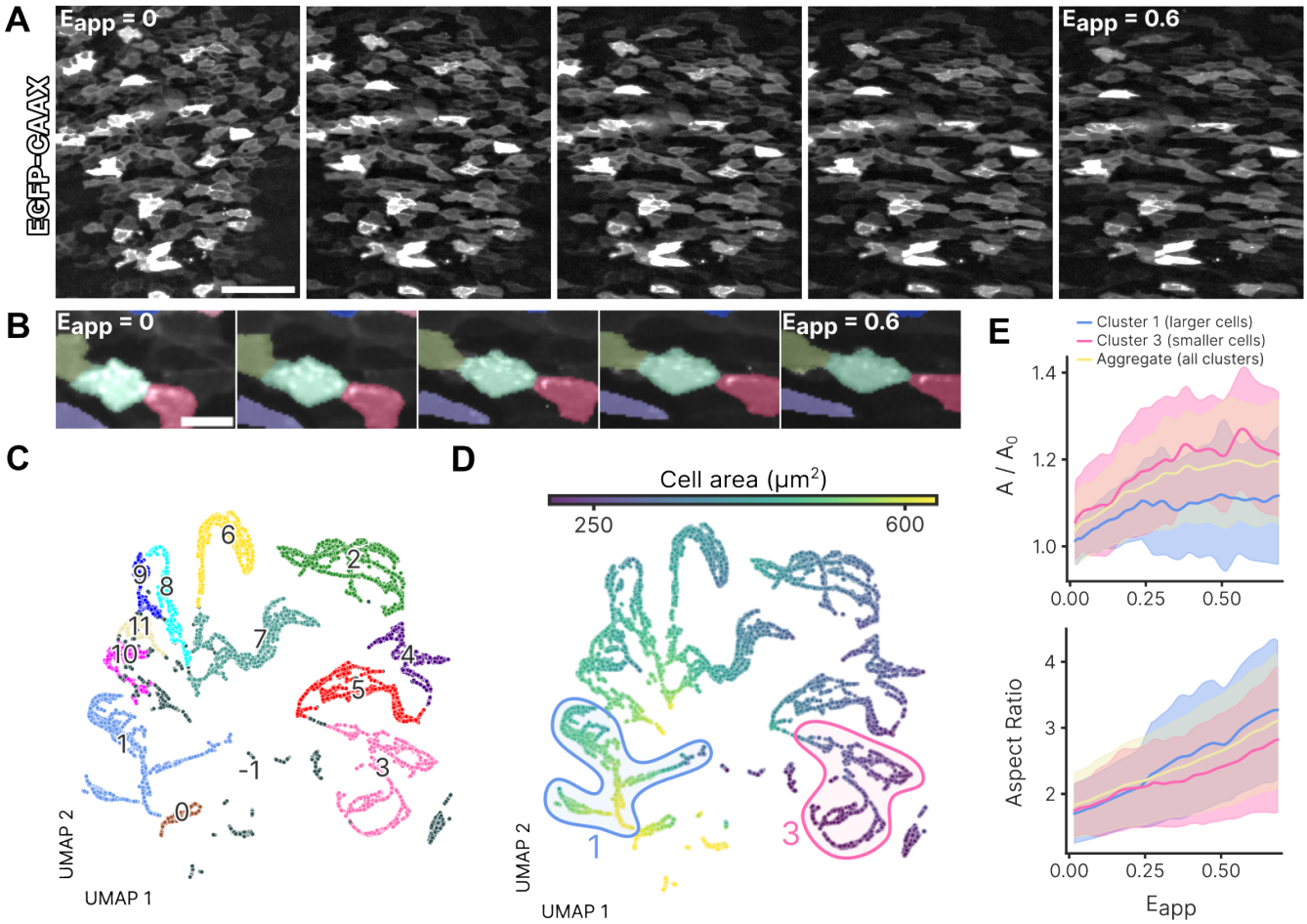

Figure 2. Cell scale response to applied strain reveals mechanotype heterogeneity. (**A**) Stills from a time lapse of EGFP-CAAX expressing endoderm cells as applied strain E_{app} is increased from 0 (left) to 0.6 (right); Scale = 100μm . (**B**) Magnified view of single cell deformation as indicated by automated segmentation and tracking as E_{app} increases from 0 (left) to 0.6 (right); Scale = 10μm (**C**) Representation of 11 distinct cell clusters identified in UMAP space; each data point indicates a single cell at a single time step during the application of exogenous stretch. (**D**) Cells in UMAP space color-coded according to their area. (**E**) Evolution of mean normalized cell area (A/A_0) (top) and aspect ratio (bottom) with increasing applied strain E_{app} for all cells, cluster 1 (large cells) and cluster 3 (small cells), and aggregate (all clusters). Solid lines indicate mean and shaded area indicates standard deviation.

RFP) (Fig. 3A, Supplemental Movie S2). Prior to stretching, F-actin disruption by DeAct-SpvB significantly decreased cell cross sectional area compared to neighboring myr-RFP expressing cells (Fig. 3B). No difference in area was observed between myr-RFP expressing cells and EGFP-CAAX expressing cells from control embryos (Fig. 3B), confirming that the effects of DeAct-SpvB on cell area were restricted to cells in which fluorescence from the GFP fused DeAct-SpvB was detected. We next examined how cell morphometrics are influenced by F-actin disruption during the application of exogenous stretch. Above, we demonstrated that cells with smaller cross sectional area are able to accommodate larger changes in area before shifting toward area-preserving deformations (Fig. S3B). We were therefore surprised to find in DeAct-SpvB-expressing cells that macroscopic stretch produced negligible changes in cell area (Fig. 3C), even though these cells began with smaller areas prior to application of exogenous strain (Fig. 3B). All the more puzzling, myr-RFP cells that neighbor DeAct-SpvB-expressing cells, but have larger areas in line with control embryos (Fig. 3B), respond to stretch similar to DeAct-SpvB cells, undergoing large deformations through cell shape changes with constant cross-sectional area (Fig. 3C). This suggests that actin disruption may have non cell-autonomous effects, altering the mechanotype of adjacent cell populations.

To examine the effects of F-actin disruption on tissue stiffness, we made use of the ability to measure applied forces in order to quantify a relative measure of tissue stiffness. Regions of endoderm where DeAct-SpvB was expressed were significantly more deformable than the equivalent region in embryos electroporated with only EGFP-CAAX (Fig. 3D). Interestingly, however, myr-RFP positive cells that neighbor DeAct-SpvB expressing cells were also highly deformable (Fig. 3D). This suggests that F-actin plays a key role in transmitting macroscopic tension in the epithelium to local cell defor-

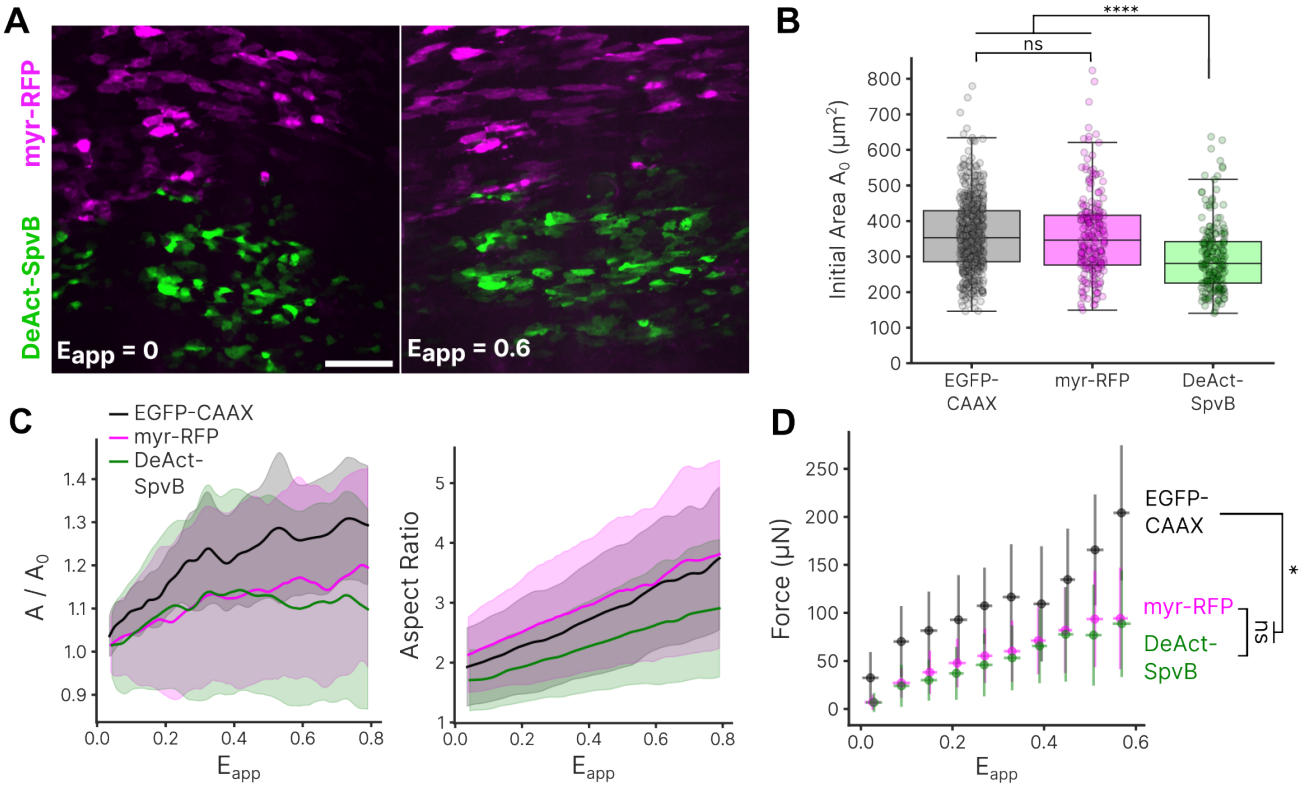

Figure 3. F-Actin disruption non-autonomously influences cell deformations and tissue stiffness in response to applied strain. (**A**) Representatives images of neighboring regions of DeAct-SpvB (green) and myr-RFP (magenta) electroporated cells before stretching (left) and at 0.6 applied strain (right); Scale = 100μm. (**B**) Area of EGFP-CAAX, myr-RFP and DeAct-SpvB electroporated cells prior to the application of exogenous stretch (One-way ANOVA followed by TukeyHSD, **** : p = 1.5e-12, ns = non significant). (**C**) Mean normalized area (left) and aspect ratio (right) for control embryos electroporated with EGFP-CAAX, compared myr-RFP and DeAct-SpvB expressing cells in dual-electroporated embryos, quantified as a function of increasing applied strain E_{app}. Solid lines indicate mean and shaded area indicates standard deviation. (**D**) Applied force quantified as a function of tissue strain for control embryos electroporated with EGFP-CAAX compared to dual electroporated embryos with strain quantified in neighboring subpopulations of myr-RFP and DeAct-SpvB expressing cells ; * : p¡0.01, ns = non-significant (One-way ANOVA followed by TukeyHSD : DeAct-SpvB vs EGFP-CAAX : p = 0.01, myr-RFP vs EGFP-CAAX : p = 0.014, DeAct-SpvB vs myr-RFP : p = 0.97).

mations, and that it may do so in a non cell autonomous manner. Further studies are needed to directly identify an underlying mechanism for these surprising results.

Stretching of endoderm *in vivo* reveals mechanical coupling between germ layers

While investigating the effects of tension on in-plane properties of the endoderm, we observed, surprisingly, that as the endoderm is stretched, subjacent somites become progressively elongated as well (Fig. 4A-C and Supplemental Movie S3). Approximately 75% of the deformation applied in the endoderm was shared by the neighboring somites, and this strain transfer between layers was largely insensitive to the magnitude of applied stretch. These data suggest that there may be a high degree of mechanical coupling between germ layers over large deformations and forces on the order of $\sim$100 μN. To test whether mesodermal deformations were the result of direct mechanical coupling, or alternatively an indirect result of tight coupling of lateral extra embryonic tissues that may dorso-ventrally compress the somites as the embryo is stretched, we examined strain transfer between germ layers following microdissection to sever the surface ectoderm, isolating the embryo proper from extra embryonic tissues along the dorsal side of the embryo (Fig. 4D). Removal of surface ectoderm did not alter strain transfer between endoderm and somites (Fig. 4D), suggesting that this phenomenon results directly from mechanical coupling across the interface between endoderm and somites. To next examine whether strain transfer exists more broadly between paraxial mesoderm and endoderm or requires apposition of basal surfaces of the endoderm and epithelialized somite boundaries, we performed similar experiments posteriorly, relying on vital dye injections to quantify tissue deformation in the presomitic mesoderm (PSM). Strain transfer was even more pronounced between endoderm and PSM, with nearly 100% of the deformation applied to the endoderm observed in the neighboring PSM (Fig. S4). This suggests that strain transfer between germ layers is not localized to somites but observed more broadly, including with mesodermal tissues that lack the organized structure of somites.

Based on previous identification of fibronectin pillars that span the space between the endoderm and somites (Sato et al., 2017), we next considered whether such extracellular matrix (ECM) components could be responsible for strain transfer. To disrupt fibronectin and collagens in the ECM, embryos were treated with dispase; mild conditions were used to sever the ECM without completely stripping it from the tissue, as more complete digestion with dispase results in delamination and severe compromise of the chick embryo (Danesin et al., 2021). Nonetheless, gentle digestion was sufficient to significantly disrupt the fibronectin-rich ECM that forms the interface between endoderm and paraxial mesoderm (Fig. 4E). Dispase treatment produced an 80% reduction in the in-plane relative stiffness of the endoderm (Fig. 4F, G). Surprisingly, however, only a modest, but significant, reduction in strain transfer was observed (Fig. 4H). These results suggest that fibronectin and collagen play a more dramatic role in determining the in-plane properties of the endodermal epithelium than they do in providing mechanical connections between the germ layers. It is possible full removal of fibronectin from the interface would have more severely reduced strain transfer, but it one cannot rule out the role of other ECM components, or cell-cell interactions across the interface as contributing to the interfacial strength between the endoderm and mesoderm.

Measurement of tensile properties of the neuroepithelium during primary neurulation

While the approach described here has been primarily developed for the study of midgut endoderm at HH stage 13, the technique can be readily extended to other stages and epithelial tissues. As a proof-of-concept, we used the stretching device to measure the forces needed to unzip the neural tube during primary neurulation. Rupture of the posterior-most adhesion point in the neural tube was achieved with pulling forces on the order of $\sim$50 μN (Fig. 5B, Supplemental Movie S4). When combined with gene misexpression and pharmacological treatments, this method could provide highly quantitative insights into the mechanobiology of neural tube zippering. These results illustrate the potentially broad applications of a relatively simple, inexpensive technique for measuring tension while applying stretch to embryonic epithelia *in vivo*.

DISCUSSION

The present study introduces a simple technique for stretching and measuring applied tension to embryonic epithelia *in vivo*. To illustrate the utility of this method, we then performed a handful of experiments aimed at understanding basic mechanical behaviors of the midgut-forming endoderm in the developing chick embryo. For example, under applied loads, we observed homogeneous strain fields at the tissue scale (Fig. 1), despite considerable mechanical heterogeneity at the single-cell level, where dimensionality reduction and clustering methods applied to cell morphometrics data revealed several distinct cell mechanotypes (Fig. 2). We found that most endoderm cells first accommodate stretch through expansion of cell area, after which area plateaus and further deformations are accommodated primarily by area-preserving shape changes (Fig. 2E). The approach can also be combined with experimental perturbations to examine how subcellular (Fig. 3) and extracellular (Fig. 4) components contribute to cell and tissue mechanics. Finally, the broader utility of this approach

was illustrated through a proof-of-concept experiment in which the forces necessary to 'unzip' the neural tube were directly measured (Fig. 5).

Our approach facilitates investigation mechanics at the length scales of both tissues and cells. Focusing first on the tissue-scale, it was somewhat surprising to see a largely homogeneous strain field upon application of exogenous stretch (Fig. 1F, G), including similar deformations between gut-forming endoderm and more lateral hypoblast cells (Fig. S1B). This suggests that tissue stiffness is similar between these cell populations, despite their disparate embryonic origins and gene expression profiles (Yasunaga et al., 2005). When considered in the context of the observed mechanical coupling between germ layers (Fig. 4), homogeneous strain fields further suggest that the endoderm may be considerably stiffer than neighboring mesodermal tissues, such that the applied tension yields similar deformations in the endoderm regardless of whether it is attached to splanchnic mesoderm, somites, intermediate mesoderm, or notochord, which vary considerably in architecture and cell type. This is further supported by the alignment of principal axes of strain with embryonic antero-posterior and medio-lateral axes, indicating that anisotropy and heterogeneity of subjacent mesodermal structures did not translate to shearing deformations in the endoderm.

Next, considering the cell response to strain, it is first worth noting that stretch was applied progressively at a rate of 0.003 mm/s, which is likely sufficiently slow to reduce confounding viscoelastic behaviors, but may be applied over too short a duration to capture force-dependent changes in cell behaviors. As such, results

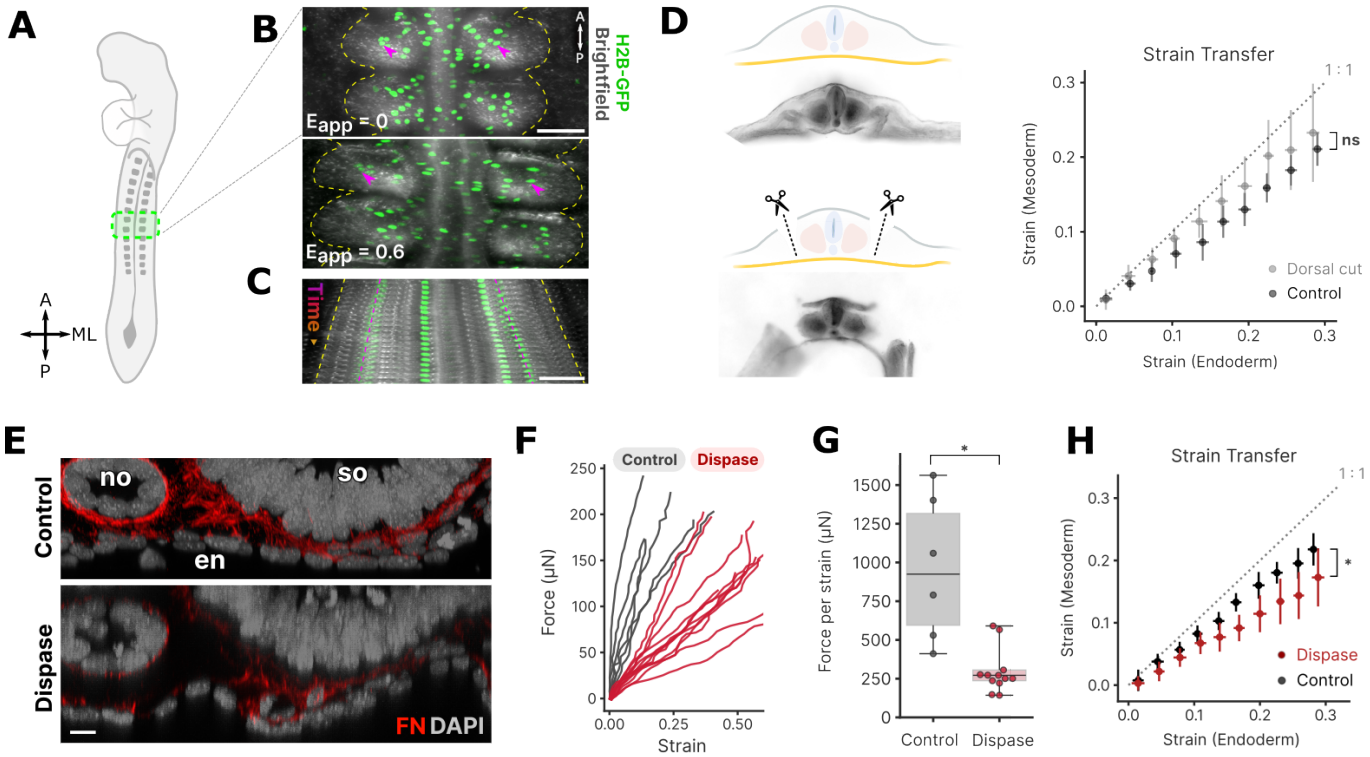

Figure 4. Mechanical coupling between endoderm and somites. (**A**) Schematic of embryonic region imaged, ventral view. (**B**) Overlay of brightfield and fluorescent images of the ventral embryo prior to (top) and after application of stretch to the endoderm (bottom); endoderm cells electroporated with pCAG-H2B-GFP (green) to visualize cell nuclei. Magenta arrows and dashed yellow lines denote the positions of two nuclei and lateral boundaries of somites as stretch is applied, respectively; Scale = 100μm. (**C**) Kymograph of stretch progressively applied to endoderm, illustrating concomitant deformation of somite boundaries as stretch is applied over time. Scale = 100μm. (**D**) To isolate mechanical interactions between endoderm and somites, microdissections were performed to sever the surface ectoderm, shown schematically and in brightfield for intact (top) and dissected (bottom) embryos. At right, Lagrangian strains are compared between the endoderm and mesoderm for control embryos and those with a dorsal cut to sever the surface ectoderm as illustrated at left; dashed grey line indicates perfect strain transfer; ns = not significant (p = 0.52, Welch's t-test on the slopes of the strain transfer per sample). (**E**) Transverse view of the endoderm-somite interface with immunostaining to visualize fibronectin (FN, red), counterstained with DAPI (grey) for control embryos (top) compared to dispase treated embryos (bottom); Scale = 10 μm. Annotations: no = notochord, so = somite, en = endoderm. (**F**) Quantification of in-plane mechanics of endoderm, illustrated by applied force vs Lagrangian strain measured in the endoderm for control and dispase-treated embryos. (**G**) Relative stiffness quantified from the slopes of force-strain curves in (F); * indicates statistical significance (p = 0.012, Welch's t-test). (**H**) Lagrangian strains are compared between the endoderm and mesoderm for control and dispase-treated embryos; dashed grey line indicates perfect strain transfer; * indicates statistical significance (p = 0.012, Welch's t-test on the slopes of the strain transfer per sample).

were largely interpreted as revealing the static, passive mechanics of cells, without capturing their biological response to tension, which may involve remodeling of cell-cell junctions (Staddon et al., 2019) and basement membrane adhesions (Kechagia et al., 2019), changes in gene expression (Panciera et al., 2017), and other more complex responses. We suspect that the tendency of most cell clusters to accommodate applied stretch first through area changes (dilatation) before shifting to area-preserving shape changes is a consequence of cells preserving their overall volume throughout deformation (Wilkes & Athanasiou, 1996): cells readily shorten their apico-basal height to accommodate in-plane stretch until the balance between incompressibility of intracellular contents and the constraints of cell-cell and cell-ECM contacts begins to favor cell shape changes that do not further alter the cell height and area. This may also explain why cells with smaller areas accommodate larger relative area changes than larger cells under exogenously applied tension (Fig. 2E and Fig. S3B), if cells within the endoderm have similar volumes at the onset of applied stretch as observed previously (Nerurkar et al., 2019).

To demonstrate the ability to measure changes in tissue mechanics upon disruption of subcellular components, we focused on F-actin, as a key structural component dictating both passive and active cell properties (Bisaria et al., 2020; Brückner et al., 2019). It was unexpected that the tendency of small cells to accommodate larger area changes (observed in EGFP-CAAX electroporated control embryos, Fig. 2) broke down upon disruption of F-actin: DeAct-SpvB-expressing cells were initially smaller (Fig. 3B), but accommodate little-to-no area increase as they deformed under exogenous stretch (Fig. 3D). This suggests that F-Actin may play an active role in coordinating apico-basal shortening to accommodate in-plane stretch (Sherrard et al., 2010). Paradoxically, however, DeAct-SpvB-expressing cells were also more deformable, reflecting the importance of actin in defining the in-plane stiffness of epithelial cells as well (Harris et al., 2012). These findings warrant further investigation, and highlight the importance of studying the mechanical response of epithelial cells *in vivo*, where complex interactions of cells with their neighbors and ECM may produce counter-intuitive results.

Mechanical interactions between germ layers have been implicated in many aspects of vertebrate morphogenesis (Smith et al., 2022), including placement of the neural anlage (Smutny et al., 2017), neurulation (Guillon et al., 2020), and axis elongation (Xiong et al., 2020). However, in most cases, these interactions have been inferred from mathematical modeling (Guillon et al., 2020), or indirectly by observing how tissue compartments respond to perturbations in the neighboring tissue (Smutny et al., 2017; Xiong et al., 2020). By developing an approach to stretch the endoderm *in vivo*, here we were able to directly test mechanical coupling between the endoderm and neighboring paraxial mesoderm (Fig. 4). Prior work by Sato, Lansford, and colleagues identified fibronectin 'pillars' extending between the basal surfaces of endoderm and somites (Sato et al., 2017) that, when perturbed, resulted in expansion of the space separating these structures. Our data support the author's assertion that fibronectin pillars contribute to mechanical interactions anchoring these tissues together, by demonstrating that across forces in the range of 10-100 μNs, strain is transferred from endoderm to somites and PSM as a linear function of applied strain. Interestingly, however, when fibronectin was partially disrupted along with collagens via dispase treatment, we only observed a moderate reduction in strain transfer (Fig. 4H). This may be due to the incomplete removal of fibronectin (Fig. 4E), but one cannot discount the potential role for direct cell-cell interactions between the endoderm and paraxial mesoderm in contributing to strain transfer as well. Unexpectedly,

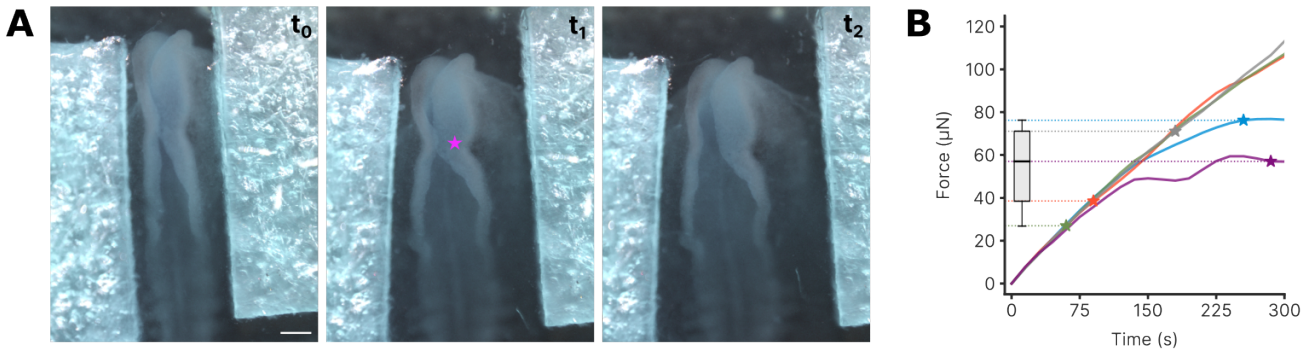

Figure 5. Measurement of forces necessary to reverse neural tube closure. (**A**) Snapshots of a HH stage 8 embryo as tension is increasingly applied across the surface ectoderm; magenta star indicates the final point of contact between the two lateral folds; Scale = 200 μm. (**B**) Measurement of the applied force as a function of time from the start of loading; stars indicate the rupture force for a given sample, and each sample is indicated by a different color.

dispase treatment had a much larger influence on the in-plane stiffness of endoderm, which was reduced by as much as 80% (Fig. 4F, G). This suggests that the ECM plays a central role in defining the passive stiffness of the endoderm, although disruption of F-actin suggests that cell contributions are also important to in-plane mechanical properties (Fig. 3D). Because events such as axis elongation and gut tube morphogenesis have traditionally been studied as mechanically distinct events, the existence of tight mechanical coupling between endoderm and paraxial mesoderm suggests that it may be necessary to reconsider these processes in the context of mechanical interactions across germ layers. For example, buffering against left-right asymmetry during somitogenesis is critical to prevent the development of scoliosis during elongation of the primary axis (Pourquié, 2011). Mechanical constraints such as somite surface tension have been implicated in size correction to maintain symmetry (Naganathan et al., 2022). In light of the present study, it is reasonable to consider whether the gut-forming endoderm plays an important mechanical role in resisting scoliotic malformations, given its tight mechanical coupling to both PSM and fully-formed somites.

MATERIALS AND METHODS

Chicken embryology techniques, electroporation and drug treatments

Fertilized White Leghorn chicken (Gallus gallus domesticus) eggs were acquired from University of Connecticut Poultry Farm and incubated at 37° C and 60% humidity for 45 hours (HH stage 12). Embryos were harvested onto filter paper rings and transferred to plates containing EC culture medium (Chapman et al., 2001). Endoderm-specific electroporation was carried out as previously described (Nerurkar et al., 2019; Oikonomou et al., 2023). Briefly, electroporation solutions were prepared by diluting pCAG-H2B-EGFP, pCAG-EGFP-CAAX (Addgene #86056), pCAG-myr-mRFP (Addgene #32604), or pCAG-DeAct-SpvB (a fusion protein of DeAct-SpvB with EGFP, subcloned into pCAG from Addgene #89446) plasmids to 3.5 μg/μL in molecular grade ddH2O with 5% sucrose and 0.1% Fast Green FCF. Following delivery of the DNA solution to the ventral surface by micropipette, embryos were electroporated using a Nepa 21 transfection system (Nepa Gene, Ichikawa City, Japan) with a sequence consisting of three 35V poring pulses of 0.2 msec duration separated by 50 msec with a decay rate of 10% between successive pulses, followed by five 4V transfer pulses of 5.0 msec duration separated by 50.0 msec with a 40% decay rate (Nerurkar et al., 2019; Oikonomou et al., 2023). Experiments were carried out after 6-8 hours incubation ex ovo, when embryos had reached HH stage 13. For the dorsal ectoderm dissections, embryos were placed dorsal side up under a Zeiss Stemi 508 stereo microscope. Using a flame-sharpened fine tungsten knife, bilaterally symmetric incisions were made to sever the surface ectoderm at the level of the posterior-most 4-5 somites. Embryos were then imaged as described below. To quantify strain in the PSM, which lacks clear discernible boundaries under brighfield, tissues were labeled by microinjection of the lipophilic dye DiI (2.5 mg/mL in DMF, Invitrogen) using pulled glass capillary needles (Fig. S4A). For dispase treatment, embryos were fitted with a small plastic confining ring to retain dispase solution, and treated with 100 μL of a 1 U/ml dispase (Dispase I protease, Sigma-Aldrich, D4818-2MG) diluted in PBS; vehicle controls similarly received 100 μl of PBS. Embryos were incubated for 10 minutes at room temperature, then rinsed in PBS, and excess moisture was wicked using a Kimwipe prior to stretching experiments.

Mechanical testing apparatus

Mechanical properties of embryonic tissues were probed using a custom micromechanical apparatus to perform uniaxial, bidirectional tensile tests. The device relies on thin tungsten rods to transmit forces to the embryo, enabling both the application of tissue strain and the measurement of the applied force (which is proportional to rod deflection, Fig. 1C, S1A). A gear system was used to achieve opposing/bidirectional displacement of a pair of tungsten rods from a single linear actuator. Each tungsten rod was afixed to a spring-loaded linear stage (Newport #460A-X), and the two stages were in turn mounted with opposing orientations on a base plate (Newport # M-BK-3A-T). One stage was directly controlled using a linear actuator (Newport #CONEX-TRA25CC), and this movement was coupled to opposing movement of the second stage using a gear system in which a centrally-positioned gear (McMaster-Carr #7880K14) rotates freely on a perpendicular rotary shaft (McMaster-Carr #1327K93) to convert rightward motion from a gear rack (McMaster-Carr #7854K11) mounted on the actuated stage into leftward motion on another gear rack that is fastened to the passive stage. On each stage, a tungsten rod of 0.005 inches diameter (A-M Systems #716000) was attached to act as the cantilever arm. Finally, stretching of the endoderm was achieved by movement of the tungsten cantilevers against filter paper squares (2 x 2 mm) placed directly on the ventral surface of the embryo; similar experiments on the neural tube were conducted by dissecting away the vitelline membrane and placing filter paper squares on the surface ectoderm to the left and right of the forming neural tube.

Bending stiffness of the tungsten cantilever was calibrated by measuring vertical deflection of the cantilever tip following hanging small pieces of aluminium foil of with known weights from the cantilever tip. Bending stiffness (0.167 N/m) was then quantified as the slope

of the force vs deflection data, as quantified by a linear regression (Fig. S1A). The tungsten cantilevers were displaced slowly at a rate of 0.003 mm/s to mitigate viscous effects. Live imaging of samples was performed as stretch was progressively applied using a ZEISS AxioZoom v16, at 50X magnification to visualize displacement of cell nuclei and 100X to visualize cell shape changes. Images were captured every 15-20 seconds for a total of 10-15 minutes or until tissue rupture. Imposed deformations were sufficiently large to warrant use of Lagrangian strains to quantify the deformation field, as opposed to linear/engineering strains. Accordingly, the tissue-scale applied strain was quantified as $E_{app} = \frac{1}{2}(\lambda^2 - 1)$, where $\lambda = L/L_0$ is the stretch ratio relating the current/deformed distance between fiducial markers near the two filter paper squares (e.g. labelled cells) normalized to their distance prior to the onset of stretch. To report the local deformations within the epithelial plane, (Fig. 1F), the full Lagrangian strain tensor was computed as $\mathbf{E} = \frac{1}{2}(\mathbf{F}^T\mathbf{F} - \mathbf{I})$, where $\mathbf{F} = \frac{\partial \mathbf{x}}{\partial \mathbf{X}}$ is the deformation gradient tensor and $\mathbf{x}$ and $\mathbf{X}$ are position vectors in the deformed and undeformed configuration, respectively. $\mathbf{F}$, and subsequently $\mathbf{E}$, were computed following the approach of (Mowlavi et al., 2022), using as input the trajectories of all cells tracked in the tissue with btrack (Ulicna et al., 2021). Direction and magnitude of principal strains were calculated by eigen-decomposition of the 2D strain tensor.

Immunofluorescence

Embryos were fixed overnight in 4% paraformaldehyde in PBS, rinsed, and dissected from surrounding extraembryonic tissue and filter paper. Embryos were washed (PBS with 0.1% Triton was used for all washes) and left in blocking solution (10% heat inactivated goat serum) for 2 hours, then incubated overnight at 4° C with mouse anti-fibronectin primary antibody (DSHB, B3/D6) diluted at 1:200. After five short 5 min washes, embryos were incubated with a goat anti-mouse 488 secondary antibody (1:200) and DAPI (1:1000) overnight. Embryos were then cleared in RapiClear (RapiClear 1.49, Sunjin Labs). Whole mount embryos stained for fibronectin (cleared, immersed in RapiClear) were imaged on a ZEISS LSM880 confocal microscope, 40X water immersion objective, with a dense z-stack at 0.2 μm spacing for optical section reconstruction.

Image analysis and Data processing

The code to follow the analysis pipeline is available on Github. Image analyses on time series movies obtained from the mechanical testing experiments were performed using the open-source image visualization Python library Napari (Sofroniew et al., 2022), preprocessing functions from the sci-kit image library (van der Walt et al., 2014), the segmentation algorithm Cellpose (Stringer et al., 2020) (starting from weights of the cyto2 model, trained with manual annotations for 1000 epochs on a workstation equipped with an NVIDIA T400 GPU), and btrack, a Python library for multi-object Bayesian tracking (Ulicna et al., 2021) (particle configuration). Where necessary, time lapse videos were stabilised against drift using custom code as in (Oikonomou et al., 2023), inspired by Fast4Dreg (Pylvänäinen et al., 2023). Cell morphometry features generated through this pipeline were aggregated across biological replicates and plotted in UMAP space, generally following the approach of cellPLATO (Shannon et al., 2023) and adapting code from ColabTracks (Jacquemet, 2024). Specifically, UMAP embedding was based on the following features: magnitude of applied strain, deformed aspect ratio, undeformed aspect ratio, current cell area, undeformed cell area, orientation of the cell major axis relative to the medio-lateral embryonic axis, minor axis length, major axis length, cell perimeter, and shape solidity (area / convex area)]. Clustering was performed on the UMAP-transformed data using HDBSCAN (McInnes et al., 2017).

Footnotes

Acknowledgments

We thank members of the Nerurkar lab for their valuable scientific input. We also thank Joseph Viola for help with designing and prototyping the mechanical stretching apparatus, and the image.sc forum users for their advice on image analysis tasks.

Author Contributions

Conceptualization: P.O., L.C., N.L.N.; Methodology: P.O., L.C., H.C., N.L.N.; Formal analysis: P.O., L.C., A.E.W. H.C., N.L.N.; Investigation: P.O., L.C., H.C., A.E.W., J.F.D., O.P., N.L.N.; Resources: N.L.N.; Data curation: P.O., L.C., A.E.W., N.L.N.; Writing – original draft: P.O., L.C., A.E.W., N.L.N.; Writing – review & editing: P.O., L.C., N.L.N.; Supervision: N.L.N.; Funding acquisition: N.L.N.

Funding

This work was funded by the NIGMS (R35GM142995, N.L.N.) with additional support from the Columbia University Digestive and Liver Disease Research Center (1P30DK132710).

Conflict of Interest

The authors have no conflict of interest to declare.

Data and Code Availability

Code to replicate the analysis can be found on Github (in the form of Python Jupyter notebooks). Representative raw image files for stretching experiments across conditions are available on Zenodo.

References

Barriga, E. H., Franze, K., Charras, G., & Mayor, R. (2018). Tissue stiffening coordinates morphogenesis by triggering collective cell migration in vivo. *Nature*, *554*(7693), 523–527. https://doi.org/10.1038/nature25742

Bisaria, A., Hayer, A., Garbett, D., Cohen, D., & Meyer, T. (2020). Membrane-proximal f-actin restricts local membrane protrusions and directs cell migration. *Science*, *368*(6496), 1205–1210. https://doi.org/10.1126/science.aay7794

Brückner, B. R., Nöding, H., Skamrahl, M., & Janshoff, A. (2019). Mechanical and morphological response of confluent epithelial cell layers to reinforcement and dissolution of the f-actin cytoskeleton [Physics meets medicine - at the heart of active matter]. *Progress in Biophysics and Molecular Biology*, *144*, 77–90. https://doi.org/https://doi.org/10.1016/j.pbiomolbio.2018.08.010

Campàs, O., Mammoto, T., Hasso, S., Sperling, R. A., O'Connell, D., Bischof, A. G., Maas, R., Weitz, D. A., Mahadevan, L., & Ingber, D. E. (2014). Quantifying cell-generated mechanical forces within living embryonic tissues [Publisher: Nature Publishing Group]. *Nature Methods*, *11*(2), 183–189. https://doi.org/10.1038/nmeth.2761

Chan, C. U., Xiong, F., Michaut, A., Vidigueira, J. M. N., Pourquié, O., & Mahadevan, L. (2023). Direct force measurement and loading on developing tissues in intact avian embryos. *Development*, *150*(9), dev201054. https://doi.org/10.1242/dev.201054

Chapman, S. C., Collignon, J., Schoenwolf, G. C., & Lumsden, A. (2001). Improved method for chick whole-embryo culture using a filter paper carrier. *Developmental Dynamics: An Official Publication of the American Association of Anatomists*, *220*(3), 284–289. https://doi.org/10.1002/1097-0177(20010301)220:3⟨284::AID-DVDY1102⟩3.0.CO;2-5

Collinet, C., & Lecuit, T. (2021). Programmed and self-organized flow of information during morphogenesis [Publisher: Nature Publishing Group]. *Nature Reviews Molecular Cell Biology*, *22*(4), 245–265. https://doi.org/10.1038/s41580-020-00318-6

Danesin, C., Ferreira, M. A., Degond, P., & Theveneau, E. (2021). Anteroposterior elongation of the chicken anterior trunk neural tube is hindered by interaction with its surrounding tissues. *Cells & Development*, *168*, 203723. https://doi.org/10.1016/j.cdev.2021.203723

Doubrovinski, K., Swan, M., Polyakov, O., & Wieschaus, E. F. (2017). Measurement of cortical elasticity in drosophila melanogaster embryos using ferrofluids [Publisher: Proceedings of the National Academy of Sciences]. *Proceedings of the National Academy of Sciences*, *114*(5), 1051–1056. https://doi.org/10.1073/pnas.1616659114

Dzementsei, A., Barooji, Y. F., Ober, E. A., & Oddershede, L. B. (2022). Foregut organ progenitors and their niche display distinct viscoelastic properties in vivo during early morphogenesis stages. *Communications Biology*, *5*(1), 402. https://doi.org/10.1038/s42003-022-03349-1

Farge, E. (2003). Mechanical induction of twist in the drosophila foregut/stomodeal primordium. *Cur-*

rent biology: CB, *13*(16), 1365–1377. https://doi.org/10.1016/s0960-9822(03)00576-1

Gómez-González, M., Latorre, E., Arroyo, M., & Trepat, X. (2020). Measuring mechanical stress in living tissues [Publisher: Nature Publishing Group]. *Nature Reviews Physics*, *2*(6), 300–317. https://doi.org/10.1038/s42254-020-0184-6

Guillon, E., Das, D., Jülich, D., Hassan, A.-R., Geller, H., & Holley, S. (2020). Fibronectin is a smart adhesive that both influences and responds to the mechanics of early spinal column development (D. Y. Stainier, T. E. Saunders, T. E. Saunders, & J. Schwarzbauer, Eds.) [Publisher: eLife Sciences Publications, Ltd]. *eLife*, *9*, e48964. https://doi.org/10.7554/eLife.48964

Harris, A. R., Peter, L., Bellis, J., Baum, B., Kabla, A. J., & Charras, G. T. (2012). Characterizing the mechanics of cultured cell monolayers. *Proceedings of the National Academy of Sciences*, *109*(41), 16449–16454. https://doi.org/10.1073/pnas.1213301109

Harterink, M., da Silva, M. E., Will, L., Turan, J., Ibrahim, A., Lang, A. E., van Battum, E. Y., Pasterkamp, R. J., Kapitein, L. C., Kudryashov, D., Barres, B. A., Hoogenraad, C. C., & Zuchero, J. B. (2017). DeActs: Genetically encoded tools for perturbing the actin cytoskeleton in single cells. *Nature methods*, *14*(5), 479–482. https://doi.org/10.1038/nmeth.4257

Jacquemet, G. (2024, January 22). CellTracksColab—a platform for compiling, analyzing, and exploring tracking data [Pages: 2023.10.20.563252 Section: New Results]. https://doi.org/10.1101/2023.10.20.563252

Kechagia, J. Z., Ivaska, J., & Roca-Cusachs, P. (2019). Integrins as biomechanical sensors of the microenvironment [Publisher: Nature Publishing Group]. *Nature Reviews Molecular Cell Biology*, *20*(8), 457–473. https://doi.org/10.1038/s41580-019-0134-2

McInnes, L., Healy, J., & Astels, S. (2017). Hdbscan: Hierarchical density based clustering. *Journal of Open Source Software*, *2*(11), 205. https://doi.org/10.21105/joss.00205

Mongera, A., Rowghanian, P., Gustafson, H. J., Shelton, E., Kealhofer, D. A., Carn, E. K., Serwane, F., Lucio, A. A., Giammona, J., & Campàs, O. (2018). A fluid-to-solid jamming transition underlies vertebrate body axis elongation [Publisher: Nature Publishing Group]. *Nature*, *561*(7723), 401–405. https://doi.org/10.1038/s41586-018-0479-2

Mowlavi, S., Serra, M., Maiorino, E., & Mahadevan, L. (2022). Detecting lagrangian coherent structures from sparse and noisy trajectory data. *Journal of Fluid Mechanics*, *948*, A4. https://doi.org/10.1017/jfm.2022.652

Naganathan, S. R., Popović, M., & Oates, A. C. (2022). Left–right symmetry of zebrafish embryos requires somite surface tension [Publisher: Nature Publishing Group]. *Nature*, *605*(7910), 516–521. https://doi.org/10.1038/s41586-022-04646-9

Nerurkar, N. L., Lee, C., Mahadevan, L., & Tabin, C. J. (2019). Molecular control of macroscopic forces drives formation of the vertebrate hindgut [Number: 7740 Publisher: Nature Publishing Group]. *Nature*, *565*(7740), 480–484. https://doi.org/10.1038/s41586-018-0865-9

Oikonomou, P., Cirne, H. C., & Nerurkar, N. L. (2023, May 18). A chemo-mechanical model of endoderm movements driving elongation of the amniote hindgut [Pages: 2023.05.18.541363 Section: New Results]. https://doi.org/10.1101/2023.05.18.541363

Panciera, T., Azzolin, L., Cordenonsi, M., & Piccolo, S. (2017). Mechanobiology of YAP and TAZ in physiology and disease [Publisher: Nature Publishing Group]. *Nature Reviews Molecular Cell Biology*, *18*(12), 758–770. https://doi.org/10.1038/nrm.2017.87

Pourquié, O. (2011). Vertebrate segmentation: From cyclic gene networks to scoliosis. *Cell*, *145*(5), 650–663. https://doi.org/10.1016/j.cell.2011.05.011

Pylvänäinen, J. W., Laine, R. F., Saraiva, B. M. S., Ghimire, S., Follain, G., Henriques, R., & Jacquemet, G. (2023). Fast4dreg - fast registration of 4d microscopy datasets. *Journal of Cell Science*, *136*(4). https://doi.org/10.1242/jcs.260728

Regev, I., Guevorkian, K., Gupta, A., Pourquié, O., & Mahadevan, L. (2022). Rectified random cell motility as a mechanism for embryo elongation. *Development (Cambridge, England)*, *149*(6), dev199423. https://doi.org/10.1242/dev.199423

Saadaoui, M., Rocancourt, D., Roussel, J., Corson, F., & Gros, J. (2020). A tensile ring drives tissue flows to shape the gastrulating amniote embryo [Publisher: American Association for the Advancement of Science]. *Science*, *367*(6476), 453–458. https://doi.org/10.1126/science.aaw1965

Sato, Y., Nagatoshi, K., Hamano, A., Imamura, Y., Huss, D., Uchida, S., & Lansford, R. (2017). Basal filopodia and vascular mechanical stress organize fibronectin into pillars bridging the mesoderm-endoderm gap. *Development*, *144*(2), 281–291. https://doi.org/10.1242/dev.141259

Savin, T., Kurpios, N. A., Shyer, A. E., Florescu, P., Liang, H., Mahadevan, L., & Tabin, C. J. (2011). On the growth and form of the gut [Publisher: Nature Publishing Group]. *Nature*, *476*(7358), 57–62. https://doi.org/10.1038/nature10277

Serra, M., Serrano Nájera, G., Chuai, M., Plum, A. M., Santhosh, S., Spandan, V., Weijer, C. J., & Ma-

hadevan, L. (2023). A mechanochemical model recapitulates distinct vertebrate gastrulation modes [Publisher: American Association for the Advancement of Science]. *Science Advances*, *9*(49), eadh8152. https://doi.org/10.1126/sciadv.adh8152

Shannon, M. J., Eisman, S. E., Lowe, A. R., Sloan, T., & Mace, E. M. (2023, October 29). *cellPLATO: An unsupervised method for identifying cell behaviour in heterogeneous cell trajectory data* (preprint). Cell Biology. https://doi.org/10.1101/2023.10.28.564355

Sherrard, K., Robin, F., Lemaire, P., & Munro, E. (2010). Sequential activation of apical and basolateral contractility drives ascidian endoderm invagination. *Current biology: CB*, *20*(17), 1499–1510. https://doi.org/10.1016/j.cub.2010.06.075

Shook, D. R., Kasprowicz, E. M., Davidson, L. A., & Keller, R. (2018). Large, long range tensile forces drive convergence during xenopus blastopore closure and body axis elongation (T. C. McDevitt, Ed.) [Publisher: eLife Sciences Publications, Ltd]. *eLife*, *7*, e26944. https://doi.org/10.7554/eLife.26944

Shyer, A. E., Tallinen, T., Nerurkar, N. L., Wei, Z., Gil, E. S., Kaplan, D. L., Tabin, C. J., & Mahadevan, L. (2013). Villification: How the gut gets its villi. *Science*, *342*(6155), 212–218. https://doi.org/10.1126/science.1238842

Smith, S. J., Guillon, E., & Holley, S. A. (2022). The roles of inter-tissue adhesion in development and morphological evolution. *Journal of Cell Science*, *135*(9), jcs259579. https://doi.org/10.1242/jcs.259579

Smutny, M., Ákos, Z., Grigolon, S., Shamipour, S., Ruprecht, V., Čapek, D., Behrndt, M., Papusheva, E., Tada, M., Hof, B., Vicsek, T., Salbreux, G., & Heisenberg, C.-P. (2017). Friction forces position the neural anlage. *Nature Cell Biology*, *19*(4), 306–317. https://doi.org/10.1038/ncb3492

Sofroniew, N., Lambert, T., Evans, K., Nunez-Iglesias, J., Bokota, G., Winston, P., Peña-Castellanos, G., Yamauchi, K., Bussonnier, M., Doncila Pop, D., Can Solak, A., Liu, Z., Wadhwa, P., Burt, A., Buckley, G., Sweet, A., Migas, L., Hilsenstein, V., Gaifas, L., … McGovern, A. (2022, May 31). *Napari: A multi-dimensional image viewer for python* (Version v0.4.16). Zenodo. https://doi.org/10.5281/zenodo.6598542

Staddon, M. F., Cavanaugh, K. E., Munro, E. M., Gardel, M. L., & Banerjee, S. (2019). Mechanosensitive junction remodeling promotes robust epithelial morphogenesis. *Biophysical Journal*, *117*(9), 1739–1750. https://doi.org/10.1016/j.bpj.2019.09.027

Stringer, C., Wang, T., Michaelos, M., & Pachitariu, M. (2020, February 3). *Cellpose: A generalist algorithm for cellular segmentation* (preprint). Bioinformatics. https://doi.org/10.1101/2020.02.02.931238

Tallinen, T., Chung, J. Y., Biggins, J. S., & Mahadevan, L. (2014). Gyrification from constrained cortical expansion. *Proceedings of the National Academy of Sciences*, *111*(35), 12667–12672. https://doi.org/10.1073/pnas.1406015111

Ulicna, K., Vallardi, G., Charras, G., & Lowe, A. R. (2021). Automated deep lineage tree analysis using a bayesian single cell tracking approach [Publisher: Frontiers]. *Frontiers in Computer Science*, *3*. https://doi.org/10.3389/fcomp.2021.734559

van der Walt, S., Schönberger, J. L., Nunez-Iglesias, J., Boulogne, F., Warner, J. D., Yager, N., Gouillart, E., Yu, T., & contributors the scikit-image, t. s.-i. (2014). Scikit-image: Image processing in python [Publisher: arXiv Version Number: 1]. https://doi.org/10.48550/ARXIV.1407.6245

Wilkes, R. P., & Athanasiou, K. A. (1996). The intrinsic incompressibility of osteoblast-like cells. *Tissue Engineering*, *2*(3), 167–181. https://doi.org/10.1089/ten.1996.2.167

Xiong, F., Ma, W., Bénazéraf, B., Mahadevan, L., & Pourquié, O. (2020). Mechanical coupling coordinates the co-elongation of axial and paraxial tissues in avian embryos. *Developmental Cell*, *55*(3), 354–366.e5. https://doi.org/10.1016/j.devcel.2020.08.007

Yasunaga, M., Tada, S., Torikai-Nishikawa, S., Nakano, Y., Okada, M., Jakt, L. M., Nishikawa, S., Chiba, T., Era, T., & Nishikawa, S.-I. (2005). Induction and monitoring of definitive and visceral endoderm differentiation of mouse ES cells. *Nature Biotechnology*, *23*(12), 1542–1550. https://doi.org/10.1038/nbt1167

Zamir, E. A., Srinivasan, V., Perucchio, R., & Taber, L. A. (2003). Mechanical asymmetry in the embryonic chick heart during looping. *Annals of Biomedical Engineering*, *31*(11), 1327–1336. https://doi.org/10.1114/1.1623487

Zhou, J., Kim, H. Y., & Davidson, L. A. (2009). Actomyosin stiffens the vertebrate embryo during crucial stages of elongation and neural tube closure. *Development (Cambridge, England)*, *136*(4), 677–688. https://doi.org/10.1242/dev.026211

SUPPLEMENTARY INFORMATION

Application of tissue-scale tension to avian epithelia *in vivo* to study multiscale mechanical properties and inter-germ layer coupling

Panagiotis Oikonomou*, Lisa Calvary*, Helena C. Cirne, Andreas E. Welch, John F. Durel, Olivia Powell, Nandan L. Nerurkar#

Department of Biomedical Engineering, Columbia University, New York NY 10027

#Correspondence to: **nln2113@columbia.edu**

351 Engineering Terrace, 1210 Amsterdam Avenue, New York, New York 10027

Supplementary Figures 1-4
Supplementary Movies 1-4

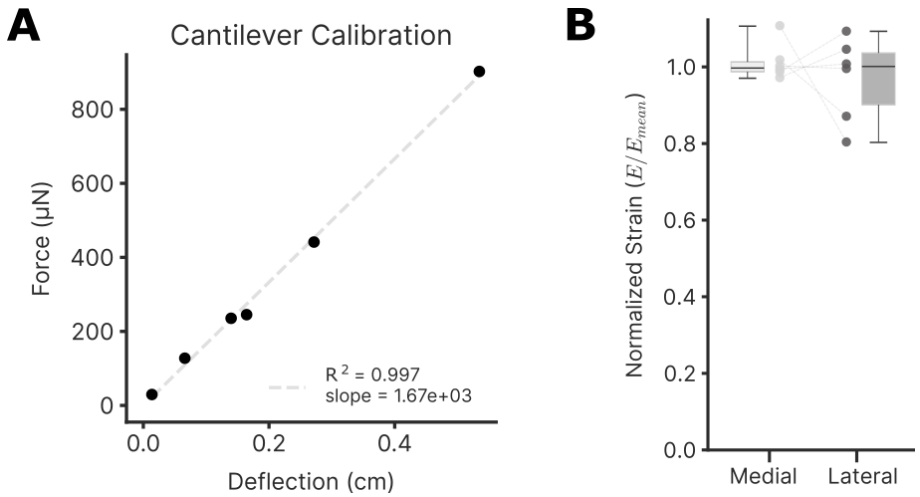

Figure S1. Beam calibration and strain heterogeneity. (**A**) Plot of cantilever deflection in function of applied force. (**B**) Paired comparison of mean normalized strains between medial (gut forming) and lateral endoderm in 6 different embryos.

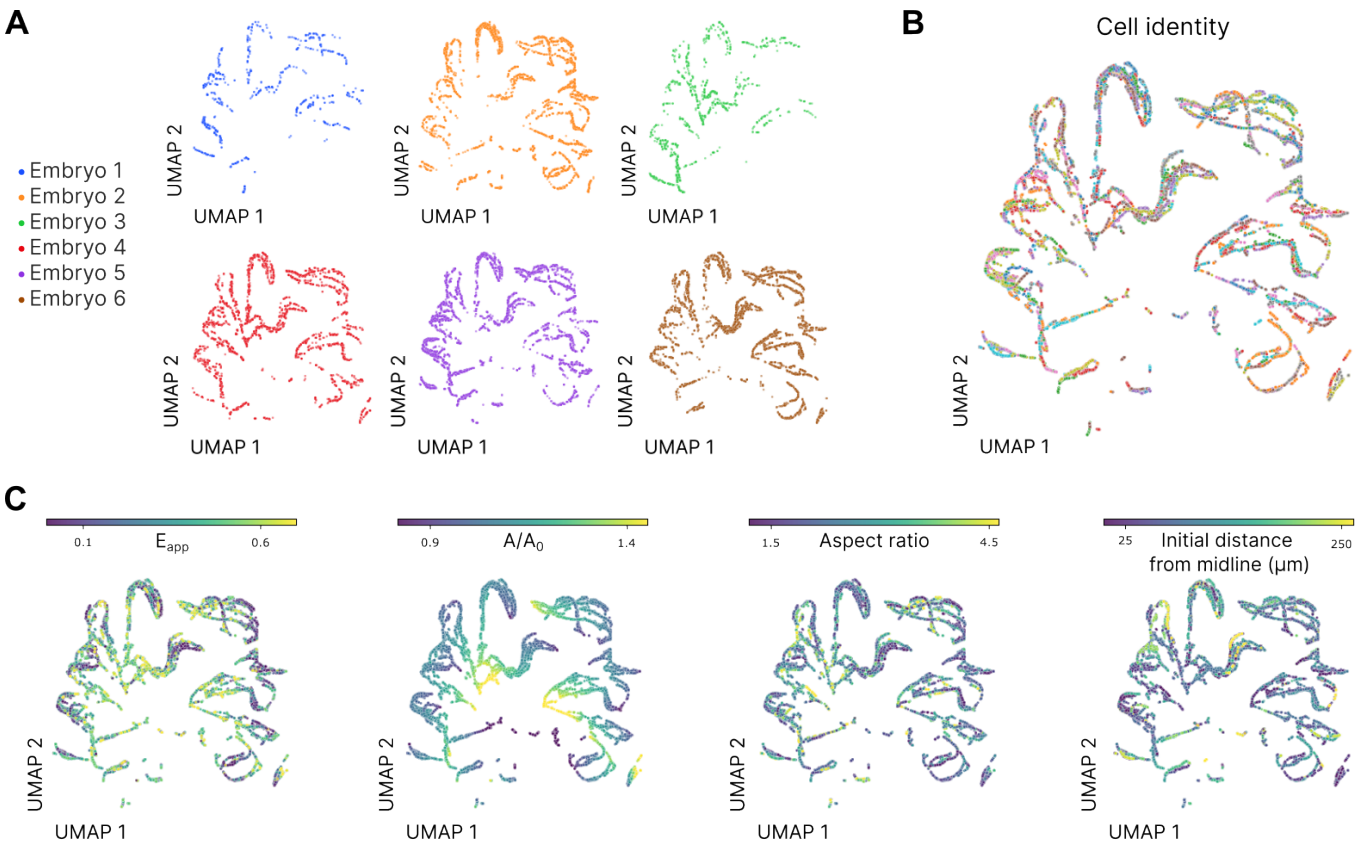

Figure S2. Distribution of cells in UMAP space. (**A**) Partitioning of cells from 6 independent experiments in UMAP space. (**B**) Visualization of cell trajectories in UMAP space by random color assignment to individual cells throughout the course of applied deformation. (**C**) UMAP color-coded according to strain, cell normalized area, aspect ratio and initial distance from midline.

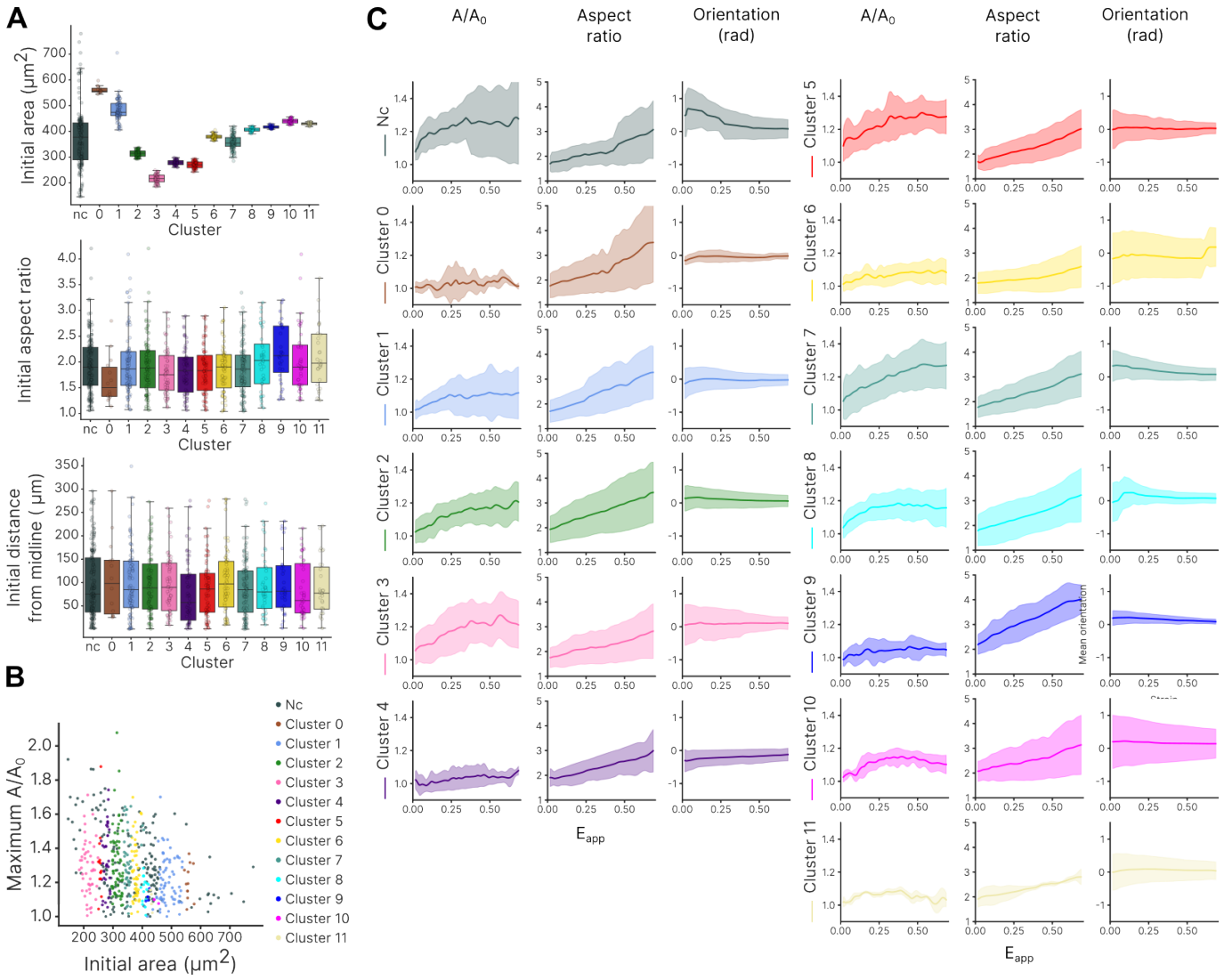

Figure S3. Evolution of morphometrics by mechanotype. (**A**) Initials features (area, aspect ratio and distance from midline) observed for the different clusters. 'Nc' correspond to cells that don't belong to any cluster. (**B**) Maximum normalized area reached as a function of initial cell area. Colors denote corresponding cluster for each cell. (**C**) Normalized area, aspect ratio and orientation as a function of applied strain for each cluster. Solid lines indicate mean and shaded area indicate standard deviation.

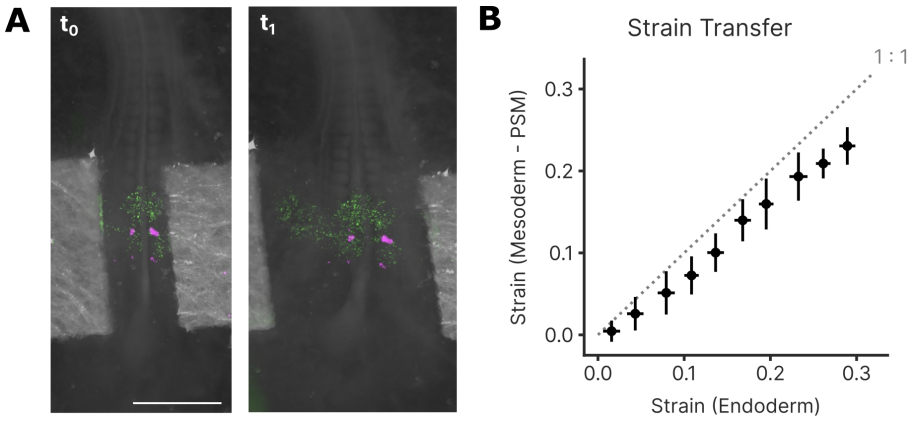

Figure S4. Strain transfer between endoderm and mesoderm is also observed at the PSM level. (**A**) Labelling strategy for tracking both endoderm (H2B-GFP electroporations, shown in green) and PSM (DiI injections, shown in magenta) deformations, showing pictures at the start (left) and at the end (right) of a stretching experiment. Scale = 1 mm. (**B**) Strain transfer plot between endoderm and mesoderm at the PSM level.

Supplementary Movie 1

EGFP-CAAX.gif
EGFP-CAAX stretch.

Supplementary Movie 2

DeAct.gif
DeAct stretch.

Supplementary Movie 3

strain_transfer.gif
Strain transfer.

Supplementary Movie 4

neural_tube.gif
Neural tube stretch.